Oriented Mesoporous Nanopyramids as Versatile Plasmon–Enhanced Interfaces

9 **AUTHORS**, INCLUDING:

Biao Kong
Monash University (Australia)
41 PUBLICATIONS 753 CITATIONS

SEE PROFILE

Cordelia Selomulya
Monash University (Australia)
130 PUBLICATIONS 1,340 CITATIONS

SEE PROFILE

Jing Wei
Monash University (Australia)
45 PUBLICATIONS 1,416 CITATIONS

SEE PROFILE

Dongyuan Zhao
Monash University (Australia)
525 PUBLICATIONS 27,495 CITATIONS

SEE PROFILE

Oriented Mesoporous Nanopyramids as Versatile Plasmon-Enhanced Interfaces

Biao Kong,[†,‡,§] Jing Tang,[†,§] Cordelia Selomulya,[‡] Wei Li,[†] Jing Wei,[†,‡] Yin Fang,[†] Yongcheng Wang,[†] Gengfeng Zheng,*[,†] and Dongyuan Zhao*[,†,‡]

[†]Department of Chemistry, Laboratory of Advanced Materials, Shanghai Key Laboratory of Molecular Catalysis and Innovative Materials, Fudan University, Shanghai 200433, P. R. China

[‡]Department of Chemical Engineering, Monash University, Wellington Road, Clayton, Victoria 3800, Australia

ⓢ Supporting Information

ABSTRACT: We developed a facile interfacial oriented growth and self-assembly process to fabricate three-dimensional (3D) aligned mesoporous iron oxide nanopyramid arrays (NPAs). The unique NPAs possess a 3D mesostructure with multiple features, including high surface area ($\sim$175 m^2/g), large pore size ($\sim$20 nm), excellent flexibility (bent over 150 times), and scalability at the foot scale for practical applications. More importantly, these NPAs structures enable versatile enhancement of localized surface plasmon resonance and photoelectrochemical conversion. The integration of plasmonic gold with 3D NPAs remarkably improves the performance of photoelectrochemical conversion, leading to $\sim$6- and 83-fold increases of the photocurrent under simulated solar and visible-light illumination, respectively. The fabrication and investigation of NPAs provide a new paradigm for preparing unconventional mesoporous oriented thin films and further suggest a new strategy for designing plasmonic metal/semiconductor systems for effective solar energy harvesting.

Direct conversion of solar energy to chemical energy using photocatalysts has received significant attention in the past decade.[1] Among numerous approaches, localized surface plasmons (LSPs), collective oscillations of conduction electrons on the surfaces of metal nanoparticles (NPs) such as Au and Ag, have been demonstrated to be capable of enhancing the efficiency of semiconductor-based photoelectrochemical (PEC) conversion devices.[2] An important goal leading toward this LSP-enhanced PEC conversion is the design and fabrication of photosynthetic materials/structures that enable effective collection of charge carriers derived from the decay of LSPs in appropriate metal–semiconductor junctions.[3,4] A major attraction of plasmonic devices is the strong morphology and geometry dependence of LSPs, in principle making it possible to design a composite plasmonic/semiconductor system that can harvest photons over a large portion of the solar spectrum.[5] Several significant aligned 3D plasmon-enhanced photoactive systems with strongly size- and shape-dependent photocatalytic activity have been reported.[6] To date, most of the 3D aligned structures, such as aligned nanopillars,[7a] nanorods,[7b] nanocones,[7c] and nanowires,[7d] are fabricated by "top-down" strategies such as reverse molding, chemical etching, and/or lithography [Figure

S1 in the Supporting Information (SI)]. On the other hand, conventional evaporation-induced self-assembly (EISA) has been shown to enable the preparation of mesostructured films.[8] Nonetheless, the EISA technique without hard templates generally requires flat surfaces for processing, mainly resulting in 2D planar mesostructured thin films.[9] Therefore, the preparation of a large-area, aligned nanoporous nanostructured film in a highly crystalline state with well-oriented frameworks, excellent accessibility, and controllable porosity is still challenging.[10]

Here we demonstrate the fabrication of oriented mesoporous nanopyramid arrays (NPAs) via an interfacial oriented growth and self-assembly process based on the van der Drift model[11] and subsequent interface-constrained thermal pyrolysis and Au deposition. The resulting plasmonic semiconductor–metal complex structures with high surface area exhibit substantially improved solar energy conversion efficiency. Briefly, highly aligned and vertically oriented coordination polymer network Prussian blue (PB) NPAs are grown on the surface of flexible titanium foil via etching-assisted hydrolysis of precursors (Figure 1). Subsequent interfacial thermal decomposition affords 3D mesoporous iron oxide NPAs, which are further coated with a
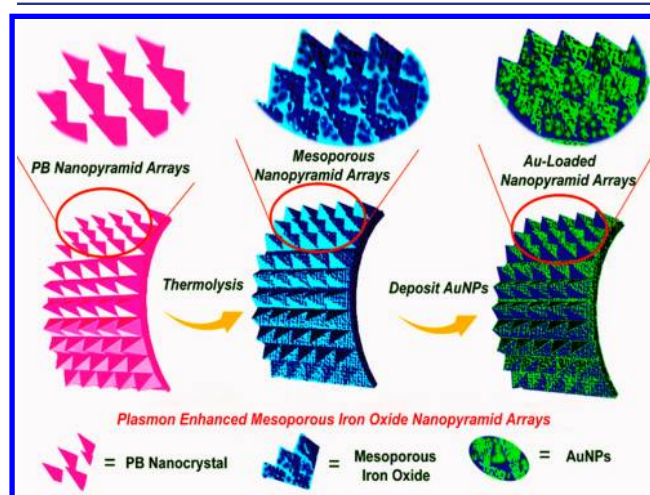

Figure 1. Schematic representation of the process to form mesoporous NPA films.

layer of Au NPs for LSP enhancement. Because of their excellent flexibility, high surface area ($\sim$175 m^2/g), and large pore size ($\sim$20 nm), the 3D mesoporous Fe$_2$O$_3$–Au NPAs exhibit substantial plasmon enhancement, in which the mesopores lead to enhancement of the PEC performance by facilitating ion transport and providing more active electrochemical reaction sites.

The interface-driven growth of the 3D NPAs is achieved by controlled hydrolysis and assembly of molecular precursors at the solution–substrate interface without structure-directing surfactants. As one of the most well-studied coordination polymers, PB has a classical cubic α-Po type network topology with the chemical formula of M$_3$[M$'$(CN)$_6$]$_2$·nH$_2$O, where M and M$'$ ions are connected to cyanide via linear M–CN–M$'$ linkages.[12] The strongly preferred {100} crystal orientation results because the fastest growth is along the ⟨100⟩ direction, in agreement with the crystal growth morphology (Figure 2a).[13] Ti
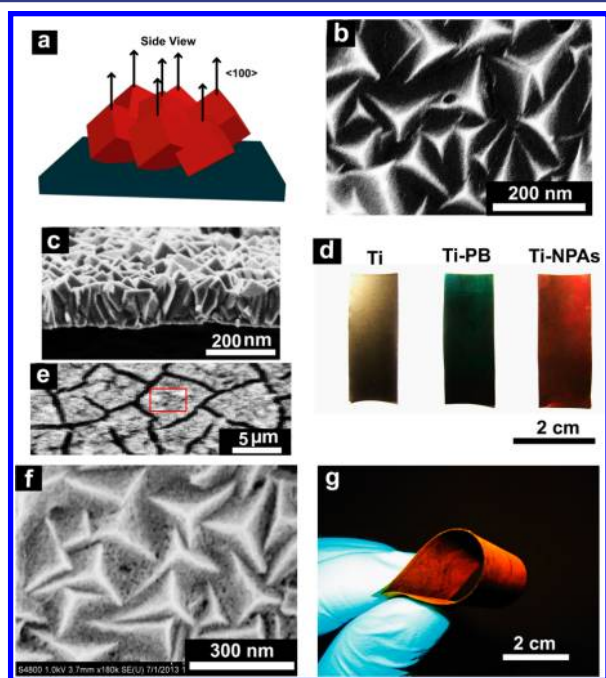
Figure 2. Structural analysis of PB and mesoporous iron oxide NPAs. (a) Microstructure of an intergrown layer of {100}-oriented PB NPAs (side view). (b, c) Top- and side-view SEM images of the obtained PB NPAs. (d) Photographs showing the colors of a bare Ti foil substrate (Ti), PB nanocrystal arrays grown on a Ti foil (Ti–PB), and mesoporous iron oxide NPAs on a Ti foil after thermolysis (Ti–NPAs). (e) SEM image of mesoporous iron oxide NPAs with islandlike aggregation and separation. (f) SEM image of a single island of mesoporous iron oxide NPAs. (g) Photograph of a bent mesoporous iron oxide NPA film revealing its flexibility and ultrathin property.

foils ($\sim$250 μm thick) with smooth surfaces (Figure S2) are used as the growth substrates for the hydrolysis of K$_3$[Fe(CN)$_6$] (see the SI for experimental details). Scanning electron microscopy (SEM) images show that the Ti foils are covered by a layer of aligned oriented nanopyramids (Figures 2b and S3). The side-view image reveals that the NPAs have a thickness of $\sim$150 nm (Figure 2c). After the synthesis, the color of the Ti foil substrate changes from silver-white to blue, suggesting the growth of Prussian blue (Figure 2d). High-resolution transmission electron microscopy (HRTEM) images show that each PB nanocube in the nanopyramid array is solid and crystalline (Figure S4). X-ray

diffraction (XRD) patterns of the bare Ti foil, the PB nanopyramid arrays on Ti foil, and PB powder show that all of the diffraction peaks are well-assigned to the face-centered-cubic Fe$_4$[Fe(CN)$_6$]$_3$ structure (Figure S5), indicating their high purity.[14] Energy-dispersive X-ray (EDX) spectra and mapping of PB NPAs reveal that the NPAs are uniformly coated with PB nanocrystals (Figure S6). In addition, the PB NPA thin film well exhibits high flexibility and stable morphology for over 150 cycles of bending and release without observable deformation (Figure S7).

After interface-constrained thermal pyrolysis, the color of the 3D NPA film changes from blue to iron red, suggesting the formation of iron oxides (Figure 2d). The mesoporous NPA films are discontinuous, with islandlike-unit-based aggregation and separation in a size of $\sim$5 μm × $\sim$5 μm (Figure 2e). The islandlike discontinuous mesoporous film can be bent easily, maintaining the excellent flexibility of the 3D structure, thus contributing to overcoming the mechanical brittleness of iron oxides (Figure S8).[15,16] An enlarged SEM image of a single island of mesoporous iron oxide NPAs shows that the PB NPAs have been transformed to iron oxide NPAs with obvious mesopores on each nanopyramid (Figure 2f). The flexibility of the mesoporous NPAs iron oxide array thin film was demonstrated by highly reversible deformation that was reproducible for over 100 cycles with a stable morphology (Figures 2g and S9). N$_2$ sorption isotherms show that the 3D NPAs have a high surface area of $\sim$175 m^2/g and a large mean pore size of $\sim$20 nm (Figure S10), and wide-angle XRD shows that they are mainly composed of α- and γ-Fe$_2$O$_3$ phases (Figure S11a).[17] X-ray photoelectron spectroscopy (XPS) analysis of the 3D NPA films demonstrates one main O$_{1s}$ peak ($\sim$533 eV) and the Fe 2p$_{1/2}$ ($\sim$725 eV) and 2p$_{3/2}$ ($\sim$710 eV) peaks in Fe$_2$O$_3$,[18] indicating that all of the films examined mainly contained Fe$_2$O$_3$ from thermolysis (Figure S11b,c).

To enhance the efficiency of mesoporous NPAs for solar energy conversion, a layer of Au nanoparticles was deposited on the 3D NPAs by sputtering. The enlarged top-view SEM image of the Fe$_2$O$_3$–Au NPAs shows that Au nanoparticles are deposited with nanoscale sizes ($\sim$5 nm) and thickness ($\sim$15 nm) on the surface of the 3D mesoporous NPAs (Figures 3a–c, S12, and S13). Ultraresolution absorption reflectance hyperspectral imaging of the mesoporous Fe$_2$O$_3$–Au NPAs was reconstructed by using an integrated CytoViva nanoscale microscope and hyper-spectral imaging system (Figure 3d). The colorful ultraresolution imaging is typically manifested in Au and 3D NPA resonances, resulting in extinction and scattering spectrum shifts. Significant resonance red shifts (74 ± 5 nm) and (152 ± 5 nm) of the absorption reflectance spectra are observed from the peak at $\sim$563 nm to 637 and 715 nm, respectively (Figure S14), in agreement with the measured UV–vis diffuse reflection spectra (Figure 3e). The absorption band (evolution of the reflection peak) of Au NPs on NPAs in the visible region increases significantly with the loading of Au NPs. This result verifies that Au NPs deposited on NPAs can significantly absorb light in the visible region, thus providing a strong basis for PEC conversion under visible-light irradiation. The 3D Fe$_2$O$_3$–Au NPAs form a typical metal–semiconductor Schottky junction.[6b,7d]

In a separate compartment, Pt wire was used as the counter electrode, at which H$_2$ evolution occurs. The resulting device is called the plasmonic electrochemical cell. To reveal the plasmon enhancement effect of Au NPs on the photoresponse of 3D Fe$_2$O$_3$ NPA electrodes, chronoamperomertic (I–t) curves for
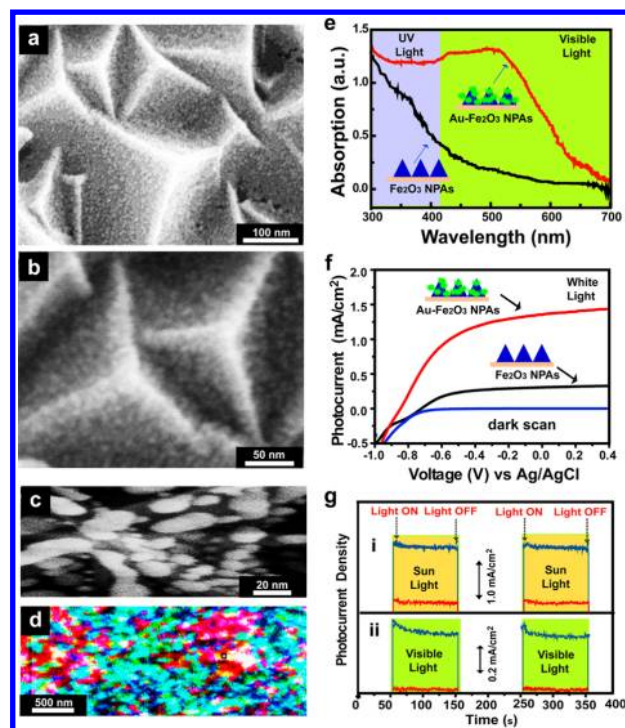
Figure 3. Characterization and PEC performance of mesoporous Au NPAs. (a−c) SEM images of the Fe_2O_3−Au NPAs. (d) Ultraresolution absorption reflectance hyperspectral imaging. (e) UV−vis diffuse reflection spectra of NPAs (black line) and Fe_2O_3−Au NPAs (red line). (f) Linear sweep voltammograms of NPA and Fe_2O_3−Au NPA electrodes recorded in 1 M KOH solution in the dark and under sunlight illumination (AM 1.5G, 100 mW/cm^2). The dark current of the Fe_2O_3−Au NPAs (blue curve) is also plotted for comparison. (g) Amperometric $I−t$ curves collected at 0.23 V vs Ag/AgCl for Fe_2O_3−Au NPA electrodes under illumination with simulated sunlight (AM 1.5G, 100 mW/cm^2) and visible light (73.3 mW/cm^2 with a 430 nm long-pass filter).

Fe_2O_3−Au NPA electrodes under simulated sunlight (AM 1.5G, 100 mW/cm^2) and visible-light illumination (by adding a 430 nm long-pass filter to the sunlight source, 73.3 mW/cm^2 with the filter). The photocurrent densities of the pristine NPA and the Au NPA electrodes are 0.21 and 1.25 mA/cm^2, respectively, at 0.23 V vs Ag/AgCl (Figure 3f). In comparison with a bare NPA electrode, the photocurrent density of Fe_2O_3−Au NPAs was increased 6-fold (0.21 to 1.25 mA/cm^2) and 83-fold (0.0056 to 0.47 mA/cm^2) at a bias of 0.23 V vs Ag/AgCl under simulated sunlight and visible-light illumination, respectively (Figure 3g). These results clearly demonstrate the significant enhancing effect of Au NPs on the PEC conversion, especially in the visible region. The sensitive enhancement effects of these nanostructures can be attributed to the plasmon−exciton interaction, which enhances light absorption and facilitates energy transfer in the NPAs.[19,20]

The proposed interfacial preferred crystal oriented self-assembly can be explained with the evolutionary selection model of van der Drift, which is commonly used to explain the oriented layer-by-layer growth of zeolites.[14c,d] The nanocrystal orientation originates from a randomly oriented seed layer on a planar surface (Figure 4a). At first, CN$^-$ ligands prefer to interact with the metal Ti foil substrate on the concave surface, and all of the seed crystals start to grow at the same time and with the same face-dependent growth rates. After a certain time that is critically dependent on the seed concentration on top of the surface, the crystals meet their lateral neighbors. Crystals that have the fastest
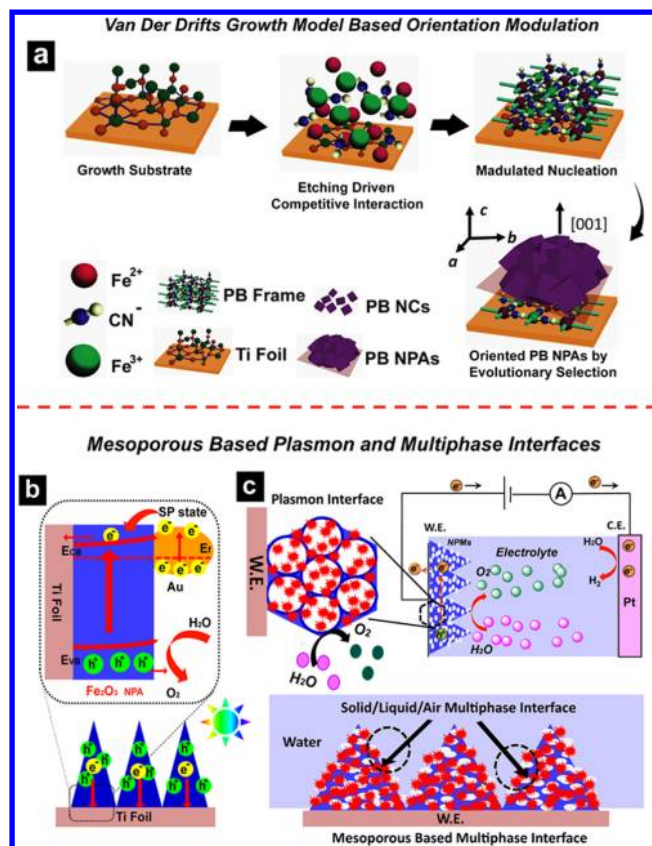
Figure 4. Schematic illustrations of synthesis and PEC conversion. (a) Proposed growth mechanism for the mesoporous NPAs. (b) Schematic energy diagram of mesoporous Fe_2O_3−Au NPAs. The expected charge-transfer directions are indicated for electrons (yellow dots) and holes (green dots). (c) Oriented mesoporous NPA-based plasmon-enhanced solid−liquid−air multiphase interfaces.

growth direction perpendicular or nearly perpendicular to the supporting surface can eventually overgrow their neighbors and form the top layer.[21] Furthermore, the growth is accomplished by the removal of adsorbed molecules and the formation of chemical bonds at the interface between nanocrystals, in which the total interfacial energy between nanocrystals decreases as a result of the elimination of the solid−liquid or solid−gas interface and the increase in total entropy.[22,23]

These spectral features of the PEC enhancement of the Fe_2O_3−Au NPAs can be attributed to generation of hot electrons and combination of the near-field plasmonic waves at the interface of 3D nanopyramids. The scheme of the fabrication steps and a schematic of the plasmonic electrochemical cell are shown in Figure 4b. Upon absorption of a photon, coherent oscillations in the free electrons are induced from Au NPs, and then a strong alternating electric field near the Au NPs is constructed. Within this system, electron−hole pairs are produced by coupling of the oscillator in the metal with the oscillator in the mesoporous NPAs. The incident-photon-to-current conversion efficiency (IPCE) of the pristine iron oxide NPAs was measured as 15−25% around 200−450 nm. In contrast, the IPCE of the Fe_2O_3−Au NPAs is significantly increased to 25−70% around 200−450 nm (Figure S14b). This plasmon-wavelength-dependent IPCE feature also verifies that excitation of the plasmon is responsible for the improved photoactivity. Furthermore, the comprehensive enhanced PEC conversion in the integrated system can be attributed to

synergistic cofactors based on well-designed 3D mesoporous nanostructures (Figure 4c), such as the large accessible pore structures, the solid−liquid−air multiphase catalytic interfaces, and their enabled fast transportation of active species and rapid electron transmission at the PEC plasmon interfaces.[24,25]

In comparison with the widely used sol−gel and EISA methods for creating 3D mesoporous structures, our method utilizes interface interactions for crystal oriented growth and subsequent mesopore formation, which has not been reported to date for transition-metal oxides.[26,27] More importantly, this approach can be conveniently scaled up to the foot scale at low cost (Figure S15), while the obtained products inherit the tailorability and flexibility of the 3D NPAs, which can be grown on a substrate and can be easily handled, cut, bent, or released without affecting their physical and chemical properties. The combination of the 3D porous nanostructure, large surface area, suitable mesopore size, and abundant surface chemistry may allow the use of 3D nanopyramid arrays for a number of applications, including PEC-based multiphase catalysis, molecule sensing, interfacial targeted recognition, and energy storage and conversion.

In summary, we have fabricated oriented mesoporous nanopyramid arrays via an interfacial oriented growth and self-assembly process based on the van der Drift model. The obtained 3D mesoporous NPAs have a high surface area (~175 m^2/g), a large mesopore size (~20 nm), and convenient scalability. Upon deposition of Au nanoparticles, the integrated plasmonic Fe_2O_3−Au NPAs exhibit significantly enhanced photoelectrochemical conversion performance, allowing for approximately 6- and 83-fold increases in the photocurrent at a bias of 0.23 V vs Ag/AgCl under simulated solar and visible-light illumination, respectively. Further development of this 3D mesoporous NPA-based fabrication and integration may open up new opportunities for a variety of plasmonic metal−semiconductor systems that can effectively harvest light for PEC-based energy applications.

■ ASSOCIATED CONTENT

Ⓢ Supporting Information

Procedures and characterization data. This material is available free of charge via the Internet at http://pubs.acs.org.

■ AUTHOR INFORMATION

Corresponding Authors

dyzhao@fudan.edu.cn
gfzheng@fudan.edu.cn

Author Contributions

§B.K. and J.T. contributed equally.

Notes

The authors declare no competing financial interest.

■ ACKNOWLEDGMENTS

■ REFERENCES

(1) (a) Tang, J.; Huo, Z.; Brittman, S.; Gao, H.; Yang, P. *Nat. Nanotechnol.* **2011**, *6*, 568. (b) Tang, J.; Kong, B.; Wang, Y.; Xu, M.; Wang, Y.; Wu, H.; Zheng, G. *Nano Lett.* **2013**, *13*, 5350.

(2) (a) Dasgupta, N. P.; Liu, C.; Andrews, S.; Prinz, F. B.; Yang, P. *J. Am. Chem. Soc.* **2013**, *135*, 12932. (b) Tao, A.; Sinsermsuksakul, P.; Yang, P. *Nat. Nanotechnol.* **2007**, *2*, 435.

(3) Thomann, I.; Pinaud, B. A.; Chen, Z.; Clemens, B. M.; Jaramillo, T. F.; Brongersma, M. L. *Nano Lett.* **2011**, *11*, 3440.

(4) Linic, S.; Christopher, P.; Ingram, D. B. *Nat. Mater.* **2011**, *10*, 911.

(5) Tada, H.; Mitsui, T.; Kiyonaga, T.; Akita, T.; Tanaka, K. *Nat. Mater.* **2006**, *5*, 782.

(6) (a) Atwater, H. A.; Polman, A. *Nat. Mater.* **2010**, *9*, 205. (b) Pu, Y.-C.; Wang, G.; Chang, K.-D.; Ling, Y.; Lin, Y.-K.; Fitzmorris, B. C.; Liu, C.-M.; Lu, X.; Tong, Y.; Zhang, J. Z. *Nano Lett.* **2013**, *13*, 3817. (c) Yu, W. J.; Liu, Y.; Zhou, H.; Yin, A.; Li, Z.; Huang, Y.; Duan, X. *Nat. Nanotechnol.* **2013**, *8*, 952. (d) Wu, Y.; Livneh, T.; Zhang, Y. X.; Cheng, G.; Wang, J.; Tang, J.; Moskovits, M.; Stucky, G. D. *Nano Lett.* **2004**, *4*, 2337.

(7) (a) Gao, H.; Liu, C.; Jeong, H. E.; Yang, P. *ACS Nano* **2012**, *6*, 234. (b) Qu, Y.; Cheng, R.; Su, Q.; Duan, X. *J. Am. Chem. Soc.* **2011**, *133*, 16730. (c) Zhu, J.; Yu, Z.; Burkhard, G. F.; Hsu, C.-M.; Connor, S. T.; Xu, Y.; Wang, Q.; McGehee, M.; Fan, S.; Cui, Y. *Nano Lett.* **2009**, *9*, 279. (d) Tian, B.; Zheng, X.; Kempa, T. J.; Fang, Y.; Yu, N.; Yu, G.; Huang, J.; Lieber, C. M. *Nature* **2007**, *449*, 885.

(8) (a) Wu, Y.; Cheng, G.; Katsov, K.; Sides, S. W.; Wang, J.; Tang, J.; Fredrickson, G. H.; Moskovits, M.; Stucky, G. D. *Nat. Mater.* **2004**, *3*, 816. (b) Meng, Y.; Gu, D.; Zhang, F.; Shi, Y.; Yang, H.; Li, Z.; Yu, C.; Tu, B.; Zhao, D. *Angew. Chem., Int. Ed.* **2005**, *44*, 7053.

(9) Feng, D.; Lv, Y.; Wu, Z.; Dou, Y.; Han, L.; Sun, Z.; Xia, Y.; Zheng, G.; Zhao, D. *J. Am. Chem. Soc.* **2011**, *133*, 15148.

(10) Tao, A. R.; Ceperley, D. P.; Sinsermsuksakul, P.; Neureuther, A. R.; Yang, P. *Nano Lett.* **2008**, *8*, 4033.

(11) Tao, A. R.; Huang, J.; Yang, P. *Acc. Chem. Res.* **2008**, *41*, 1662.

(12) Ferlay, S.; Mallah, T.; Ouahes, R.; Veillet, P.; Verdaguer, M. *Nature* **1995**, *378*, 701.

(13) Keggin, J.; Miles, F. *Nature* **1936**, *137*, 577.

(14) (a) Uemura, T.; Kitagawa, S. *J. Am. Chem. Soc.* **2003**, *125*, 7814. (b) Buser, H.; Schwarzenbach, D.; Petter, W.; Ludi, A. *Inorg. Chem.* **1977**, *16*, 2704. (c) Li, Y. S.; Bux, H.; Feldhoff, A.; Li, G. L.; Yang, W. S.; Caro, J. *Adv. Mater.* **2010**, *22*, 3322. (d) Bux, H.; Feldhoff, A.; Cravillon, J.; Wiebcke, M.; Li, Y.-S.; Caro, J. *Chem. Mater.* **2011**, *23*, 2262.

(15) Lu, X.; Zhai, T.; Zhang, X.; Shen, Y.; Yuan, L.; Hu, B.; Gong, L.; Chen, J.; Gao, Y.; Zhou, J. *Adv. Mater.* **2012**, *24*, 938.

(16) Wang, G.; Zhang, L.; Zhang, J. *Chem. Soc. Rev.* **2012**, *41*, 797.

(17) Hu, M.; Belik, A. A.; Imura, M.; Mibu, K.; Tsujimoto, Y.; Yamauchi, Y. *Chem. Mater.* **2012**, *24*, 2698.

(18) Dong, X.; Chen, H.; Zhao, W.; Li, X.; Shi, J. *Chem. Mater.* **2007**, *19*, 3484.

(19) Snaith, H. J.; Moule, A. J.; Klein, C.; Meerholz, K.; Friend, R. H.; Grätzel, M. *Nano Lett.* **2007**, *7*, 3372.

(20) Grätzel, M. *Nature* **2001**, *414*, 338.

(21) (a) Xu, G.; Yamada, T.; Otsubo, K.; Sakaida, S.; Kitagawa, H. *J. Am. Chem. Soc.* **2012**, *134*, 16524. (b) Liu, B.; Shekhah, O.; Arslan, H. K.; Liu, J.; Wöll, C.; Fischer, R. A. *Angew. Chem., Int. Ed.* **2012**, *51*, 807. (c) Schoedel, A.; Scherb, C.; Bein, T. *Angew. Chem., Int. Ed.* **2010**, *49*, 7225.

(22) Penn, R. L.; Banfield, J. F. *Science* **1998**, *281*, 969.

(23) Penn, R. L. *J. Phys. Chem. B* **2004**, *108*, 12707.

(24) Feng, D.; Luo, W.; Zhang, J.; Xu, M.; Zhang, R.; Wu, H.; Lv, Y.; Asiri, A. M.; Khan, S. B.; Rahman, M. M. *J. Mater. Chem. A* **2013**, *1*, 1591.

(25) Hochbaum, A. I.; Yang, P. *Chem. Rev.* **2010**, *110*, 527.

(26) Wan, Y.; Zhao, D. *Chem. Rev.* **2007**, *107*, 2821.

(27) Deng, Y.; Wei, J.; Sun, Z.; Zhao, D. *Chem. Soc. Rev.* **2013**, *42*, 4054.